RSC Advances

PAPER

View Article Online
View Journal | View Issue

Cite this: *RSC Adv.*, 2026, **16**, 23391

Rapid, point-of-care, visual detection of RBD of SARS-CoV-2 spike protein using an acrylamide-free photonic crystal aptasensor

Meghana Mary Thomas,[ac] Parvathy R. Chandran,[a] Lekshmi Lekshmanan,[bc] A. Peer Mohamed[a] and Saju Pillai *[ac]

As COVID-19 continues to reemerge with new variants, it has become a persistent challenge to public health, causing disruptions in society and the economy. We report a facile photonic crystal-based aptasensor for the rapid visual detection of the receptor-binding domain (RBD) of the severe acute respiratory syndrome (SARS-CoV-2) spike (S) protein. Monodispersed polystyrene@poly(2-hydroxyethyl methacrylate–acrylic acid) [PS@poly(HEMA–AA)] core–shell microspheres were synthesized to fabricate a stimuli-responsive photonic crystal (RPC). The integration of the RBD target-specific aptamer into the poly(HEMA–AA) hydrogel network facilitated the development of a biosensor that enabled RPCs to selectively bind to the SARS-CoV-2 spike protein using coupling chemistry. The interaction between the RBD and a single-stranded DNA aptamer causes the hydrogel to expand, leading to a color change and a shift in the photonic bandgap (PBG). This phenomenon can be used to detect the RBD of the SARS-CoV-2 spike protein. The addition of the RBD of SARS-CoV-2-S-protein to the Apt-RPC aptasensor resulted in a rapid visual color shift from violet to green. The detection range of the developed aptasensor was estimated to be 100–1000 ng with excellent selectivity. Thus, the developed aptasensor offers distinct advantages over conventional detection methods. Our study also facilitates the development of a straightforward point-of-care self-testing kit that does not rely on toxic acrylamide-based chemicals. Furthermore, the sensor eliminates the need for complex sample preparation or signal amplification steps, making it a promising platform for point-of-care diagnosis.

Received 14th February 2026
Accepted 27th April 2026

DOI: 10.1039/d6ra01315e

rsc.li/rsc-advances

Introduction

The severe acute respiratory syndrome coronavirus 2 (SARS-CoV-2) pandemic that broke out in 2019 (COVID-19) has had a devastating impact on people's livelihoods, economy, and social life at large.[1–6] According to the World Health Organization (WHO), COVID-19 has affected 778 million people worldwide and has led to 7 million deaths worldwide.[7] SARS-CoV-2 has mutated into multiple variants and sub-variants, including, but not limited to, alpha, beta, gamma, delta, epsilon, omicron, and the latest XEC variant, and continues to spread among individuals with enhanced transmissibility and virulence.[8–10] Currently, reverse transcription polymerase chain reaction (RT-PCR) using gold as the standard is the predominant method for the detection of SARS-CoV-2, although it is time-consuming. However, rapid on-site diagnosis of SARS-CoV-2 is impeded by intricate sample handling protocols, the need for skilled personnel, and prolonged detection time.[11,12] Alternatively, colloidal gold immunochromatography and antigen-based enzyme-linked immunosorbent assays (ELISA) are qualitative detection methods for SARS-CoV-2.[13,14] According to several studies, the receptor-binding domain (RBD) of the SARS-CoV-2 spike glycoprotein (S-protein) mediates viral cell entry and disease progression. The RBD of the SARS-CoV-2 S-protein infiltrates human respiratory and digestive epithelial cells *via* angiotensin-converting enzyme II (ACE2), which plays a key role in the diagnosis and treatment of SARS-CoV-2.[15,16] However, the bio-recognition components of most S-protein detection methods use antibodies or ACE-2 enzymes, and their synthesis protocols are time-consuming and involve the exploitation of animal models. Moreover, these methods are expensive, and proteins may be denatured when exposed to elevated temperatures or pH fluctuations.[17,18] Therefore, the development of a facile RBD-based approach could serve as a viable option for the rapid, cost-effective PoC diagnosis of SARS-CoV-2 infection.

Aptamers are an alternative to antibodies for the detection of the SARS-CoV-2 S protein. They are small, single-stranded DNA or RNA molecules that selectively bind to specific targets, including

[a]*Materials Science and Technology Division, CSIR-National Institute for Interdisciplinary Science and Technology (NIIST), Thiruvananthapuram 695 019, India. E-mail: pillai_saju@niist.res.in*

[b]*Chemical Sciences and Technology Division, CSIR-National Institute for Interdisciplinary Science and Technology (NIIST), Thiruvananthapuram 695 019, India*

[c]*Academy of Scientific and Innovative Research (AcSIR), Ghaziabad 201 002, India*

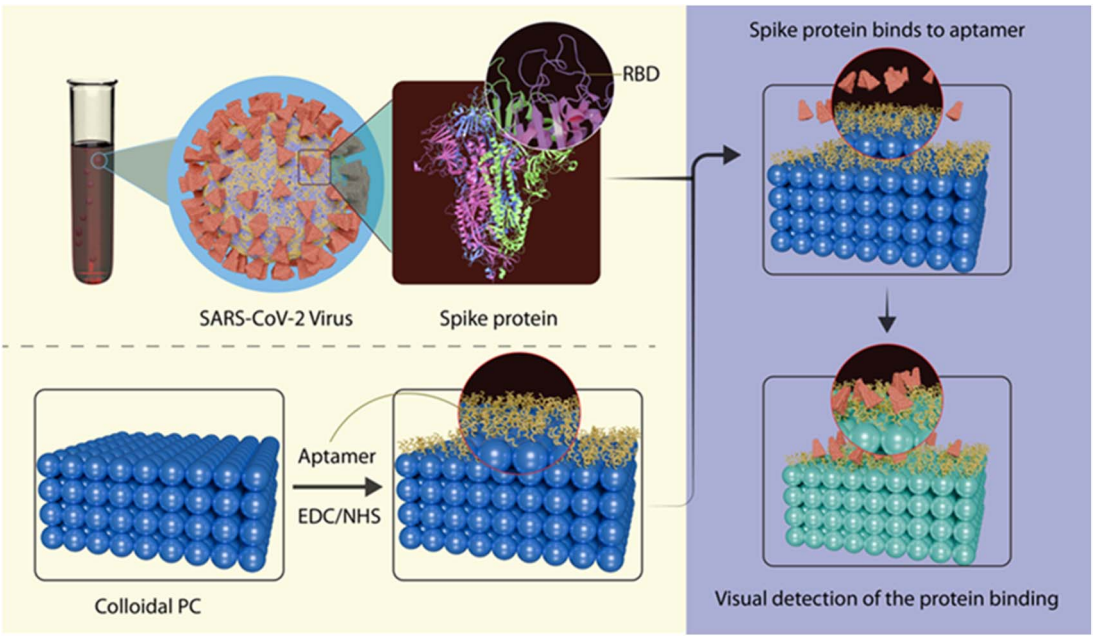

Scheme 1 Schematic illustration of the aptasensor RPC for the rapid detection of RBD of the SARS-CoV-2 spike protein.

peptides, proteins, carbohydrates, small toxins, and live cells.[19–23] Compared to antibodies, the smaller size of aptamers causes less hindrance to the surface of the virus. In addition, they are stable, cost-effective, possess negligible batch-to-batch variation, and are convenient for transportation.[24] Aptamers with affinity for a specific target can be generated *via* the SELEX approach, which implies the successive evolution of ligands by exponential enrichment using a vast oligonucleotide library.[25] Thus, aptamer-based sensors represent an effective therapeutic and prophylactic approach for controlling SARS-CoV-2 infection and potential future pandemics.

Integrating aptamers into responsive photonic crystals (RPCs) is an efficient method for analyte detection.[26–31] They can shift the photonic bandgap (PBG) through a volume phase transition (swelling/deswelling) under external stimuli. Based on the variation in lattice spacing, RPCs display a blue or red shift in the PBG position, and the resultant structural color changes enable label-free visual detection of analyte molecules.[32–36] Ye *et al.* reported aptamer-functionalized RPCs for the visual detection of heavy metal ions.[37] Xuan *et al.* demonstrated aptasensor functionalized with P(NIPAM–AA) hydrogel, which is a one-dimensional CPCs, for the colorimetric detection of heavy metal ions.[38] The hydrogel network embedded in CPCs shrinks owing to the specific binding of heavy metal ions to the functionalized single-stranded aptamer, which alters the lattice spacing and causes a blue shift in the PBG. Similarly, Murtaza *et al.* reported a photonic crystal-based aptasensor that requires a complex fabrication procedure, limiting its scalability for the detection of SARS-CoV-2.[39] Nevertheless, a simple approach using smart core–shell polymer microspheres of 3D CPCs with the desired functionalities to modulate the PBG within the visible-light region has not been explored for SARS-CoV-2 S-protein detection.

In the present work, we demonstrate RPCs that are more specific to an analyte by attaching the aptamer sequence to the hydrogels through 1-ethyl-3-(3-dimethyl aminopropyl)carbodiimide (EDC)/*N*-hydroxysuccinimide (NHS) coupling. The designed biosensor integrates the benefits of RPCs and aptamers, providing an efficient and scalable approach for SARS-CoV-2 RBDs detection. We synthesized PS@poly(HEMA–AA) core–shell microspheres *via* emulsifier-free emulsion polymerization and employed them to fabricate 3D CPCs using a vertical deposition method.[40] The rigid PS core imparts structural stability, whereas the soft hydrogel shell contributes to stimuli-responsive characteristics. An aptamer targeting the SARS-CoV-2 RBD was functionalized onto the carboxylic functional group of the hydrogel shell *via* EDC/NHS chemistry. The specific binding of RBD to a single-stranded DNA aptamer causes swelling of the hydrogel, and the corresponding red shift in the PBG was used to detect the SARS-CoV-2 S-protein (Scheme 1).

Results and discussion

Synthesis and characterization of PS@poly(HEMA–AA) microspheres

Monodispersed PS@poly(HEMA–AA) core–shell microspheres were synthesized *via* emulsifier-free emulsion polymerization. Based on the differences in polarity and hydrophilicity of the co-monomers, the polymerization reaction resulted in the formation of core–shell microspheres with less polar, hydrophobic PS as the core and hydrophilic poly(HEMA–AA) as the shell. Acrylic acid imparts carboxylic functionality to the surface of CS microspheres. Fig. 1A shows the dynamic light scattering (DLS) results of the synthesized particles with an average hydrodynamic diameter of 195 nm and a polydispersity index (PDI) of 0.014, indicating the formation of monodispersed microspheres. The

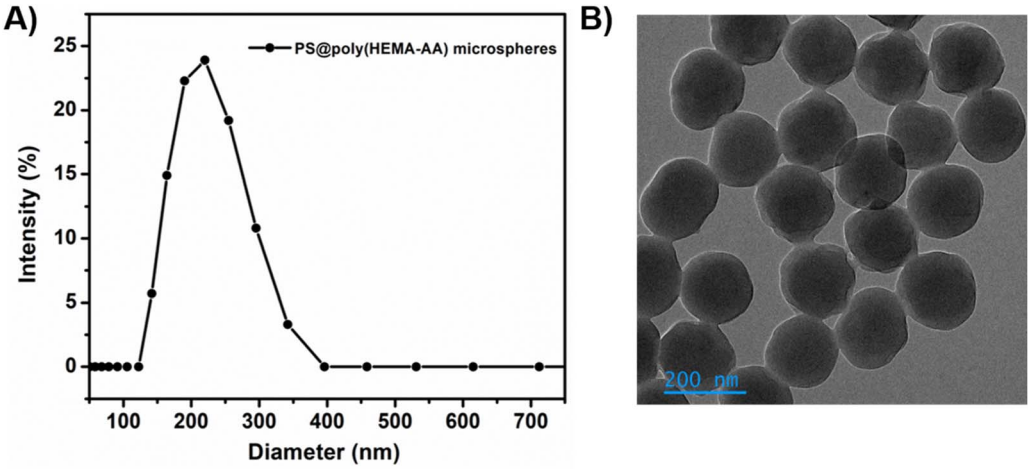

Fig. 1 (A) DLS plot and (B) TEM image of PS@poly(HEMA–AA) microspheres.

zeta potential value of the solution was −42.7, suggesting the formation of stable colloid. Fig. 1B presents the TEM image of the PS@poly(HEMA–AA) microspheres, where the darker core corresponds to the PS and the lighter area represents the poly(HEMA–AA) shell. The average diameter of the microspheres was 168 ± 10 nm, with a shell thickness of 40 ± 10 nm.

The chemical functionality of the synthesized microspheres was analyzed using FT-IR. The IR spectrum of the PS@poly(-HEMA–AA) microspheres (Fig. 2A) shows characteristic peaks of polystyrene (PS) at 3065 cm^{-1}, 3023 cm^{-1} indicating the aromatic C–H stretching vibrations, peaks at 1600 cm^{-1}, 1489 cm^{-1}, and 1449 cm^{-1} representing aromatic C=C stretching vibrations, aromatic out-of-plane C–H bending at 758 cm^{-1}, and the band at 699 cm^{-1} corresponding to aromatic ring bending. Furthermore, the peak at 1719 cm^{-1} indicates the carbonyl stretching frequency of the poly(HEMA–AA) shell, whereas a larger peak near 3435 cm^{-1} represents the O–H stretching vibration of pHEMA. The peaks at 1165 cm^{-1} and

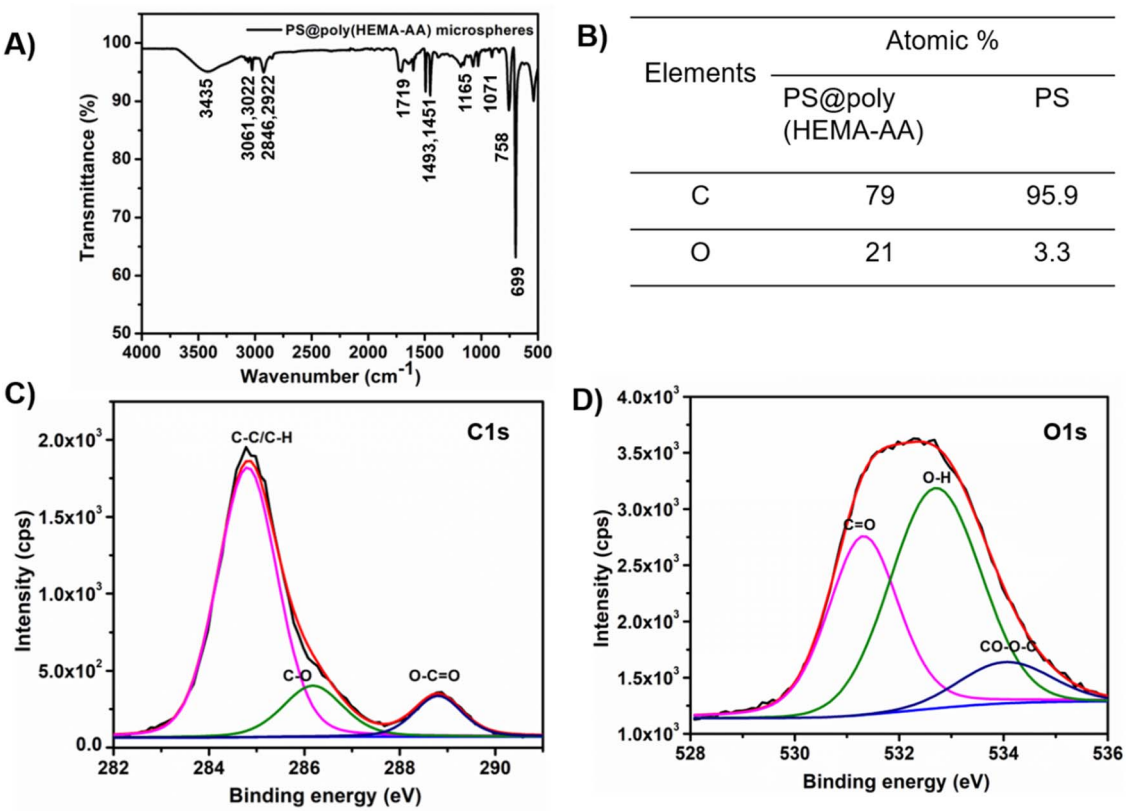

Fig. 2 (A) FT-IR spectrum of PS@poly(HEMA–AA) microspheres, (B) elemental composition of PS@poly(HEMA–AA) and PS microspheres, (C) XPS C 1s narrow scan, and (D) XPS O 1s narrow scan of PS@poly(HEMA–AA) microspheres.

1071 cm^{-1} indicate C–O–C antisymmetric and stretching vibrations, respectively, from pHEMA and pAA. These peaks indicate the formation of a poly(HEMA–AA) shell. XPS was used to investigate the surface chemistry of the PS@poly(HEMA–AA) microspheres. The elemental compositions of the PS and PS@poly(HEMA–AA) microspheres obtained from the XPS survey spectra are summarized in Fig. 2B. Compared to the PS microspheres, the CS microspheres exhibited increased oxygen elemental content, which could indicate the formation of a poly(HEMA–AA) hydrogel in the shell. The deconvoluted XPS C 1s narrow scan of the PS@poly(HEMA–AA) microsphere (Fig. 2C) revealed three components with binding energies of 284.8, 286.2, and 288.8 eV, corresponding to C–C/C–H, C–O, and O–C=O, respectively. Peaks at binding energy values of 531.3, 532.7, and 534 eV, corresponding to C=O, O–H, and CO–O–C, respectively, were apparent in the deconvoluted spectrum of the XPS O 1s narrow scan (Fig. 2D). Therefore, the existence of the poly(HEMA–AA) shell was confirmed by the XPS results.

Fabrication of PS@poly(HEMA–AA)-based stimuli-RPCs

In contrast to conventional PS microsphere-based CPC synthesis, the integration of a hydrophilic shell into PS microspheres facilitates volume phase transitions *via* hydrogel swelling or deswelling, making it an efficient approach for the development of stimuli-responsive photonic crystals (RPCs).[41,42] Here, the rigid PS core imparts structural stability, whereas the soft poly(HEMA–AA) hydrogel shell contributes to the stimuli-responsive characteristics. PS@poly(HEMA–AA) microspheres were used to fabricate RPC on a pre-cleaned hydrophilic glass substrate *via* evaporation-induced vertical deposition. The UV-vis reflectance spectrum (Fig. 3A) shows the PBG position centered at 449 nm, and the inset of Fig. 3A depicts its characteristic structural color, bright violet. In Fig. 3B, the corresponding CIE plot is presented. The SEM micrograph of RPC revealed a well-ordered, closely packed arrangement of PS@poly(HEMA–AA) microspheres, as illustrated in Fig. 3C.

Fabrication of aptasensor-based on RPC (Apt-RPC) for sensing RBD of SARS CoV-S-protein

In RPCs, stimuli-responsive hydrogels can either swell or deswell in response to the analyte molecule, thus altering the center-to-center spacing between adjacent colloidal particles, which causes a shift in the structural color.[43] This shift in the color of RPCs in response to external stimuli can be employed for the visual detection of analytes in biosensing applications. A photonic crystal-based aptasensor (Apt-RPC) was fabricated by functionalizing PS@poly(HEMA–AA) microspheres with RBD-selective single-stranded DNA aptamer *via* EDC-NHS coupling chemistry. The designed aptamer was directly functionalized by the carboxylic acid group present in the poly(-HEMA–AA) shell. Scheme 1 depicts the covalent coupling of aptamers with the carboxyl group of poly(HEMA–AA) microspheres. The specific binding of Apt-RPC to RBD alters the periodicity of RPC. This study utilized the aptamer sequence reported by Song *et al.*, identified through an ACE2 competition-based selection strategy and a machine learning screening algorithm that selectively binds the RBD of SARS-CoV-2 S-protein with a K_d value of 5.8 nM.[44] The selected aptamer sequence was 5′-CAG CAC CGA CCT TGT GCT TTG GGA GTG CTG GTC CAA GGG CGT TAA TGG ACA-3, with 51 bases and a hairpin structure. To prepare Apt-RPC, the PS@poly(HEMA–AA) core–shell was activated with an EDC-NHS solution for 1 h at room temperature. The aptamer solution was added, incubated at room temperature for 30 min, and then refrigerated overnight at 4 °C. The functionalization of aptamers to poly(HEMA–AA) hydrogel shells *via* amide bonds (–CO–NH–) was confirmed using XPS analysis. The XPS survey spectrum of the Apt-RPC sample revealed that C, O, and N were the major constituents. Compared to RPC, the presence of an additional element, nitrogen, arises from the aptamer bonded to the poly(HEMA–AA) hydrogel shell. The deconvoluted XPS narrow scan of C 1s (Fig. 4A) revealed the presence of C=C, C–C, C–N, C–O, and O–C=O bonds with binding energies of 283.5, 284.8, 285.1, 286.5, and 288.5 eV, respectively. The presence of a C–N bond can be attributed to the formation of an amide bond. The deconvoluted XPS narrow scan N 1s (Fig. 4B) indicates the existence of C–N, N–C=O, and N–H with binding energies of 397.5, 398.6, and 401.8 eV, respectively. Fig. 4C presents an SEM micrograph of an ordered and close-packed arrangement of Apt-RPCs, suggesting the structural stability of the RPC sample even after aptamer functionalization. The PBG of CPC follows modified Bragg's law, where,

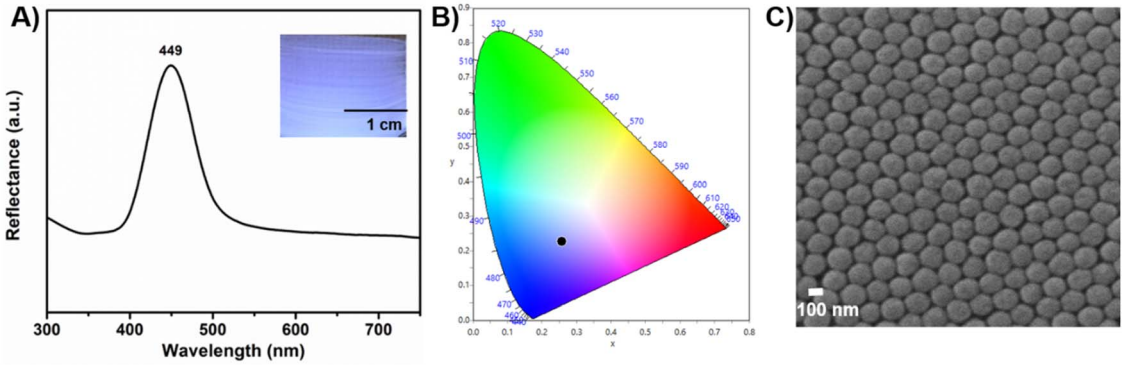

Fig. 3 (A) Reflectance spectra and digital photograph (inset), (B) CIE plot, and (C) SEM image of the fabricated PS@poly(HEMA–AA) RPC.

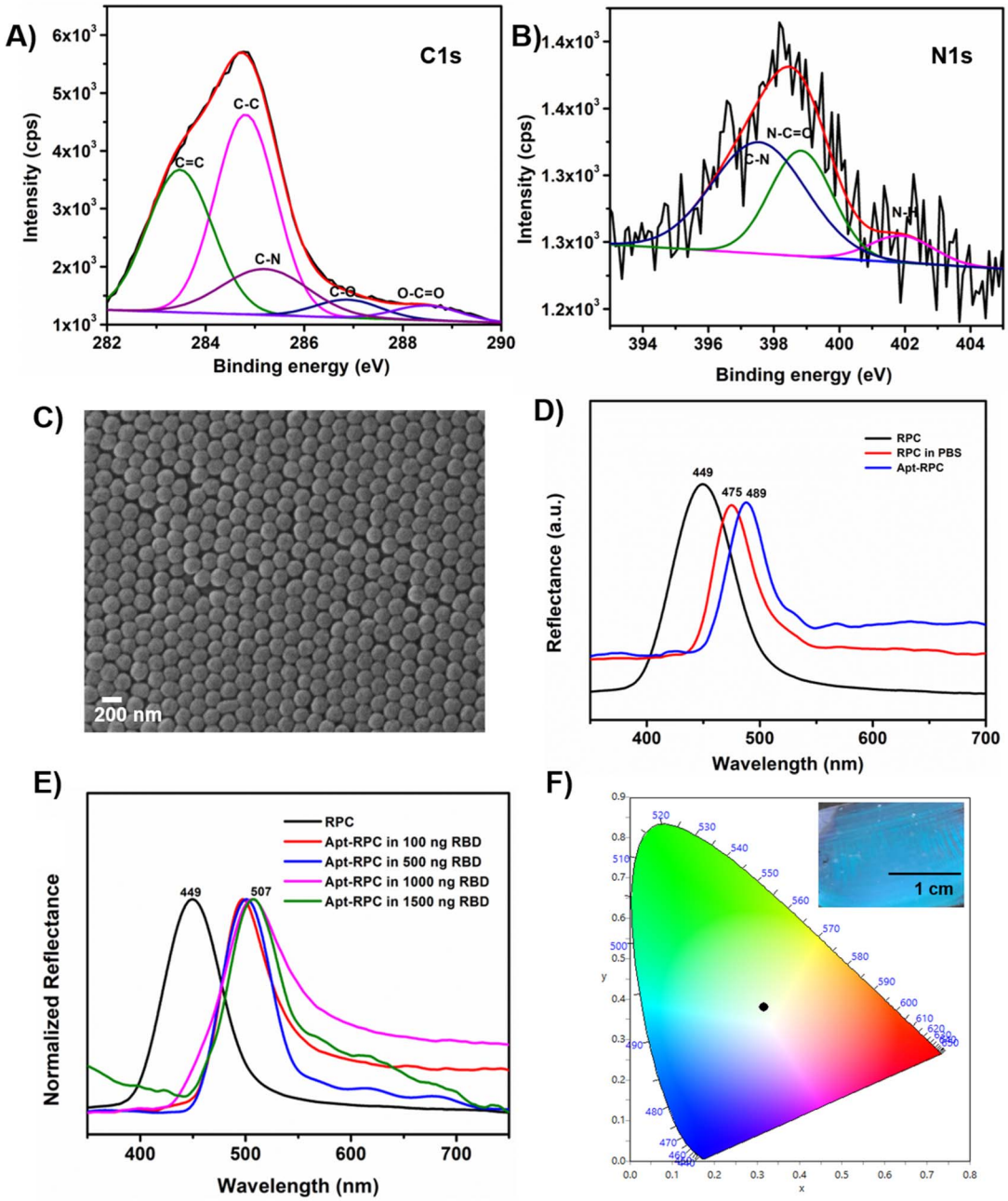

Fig. 4 (A) XPS C 1s and (B) N 1s narrow scans of Apt-RPC, (C) SEM micrograph of Apt-RPC, (D) reflectance spectra of RPC, RPC in PBS solution (pH 7.4), and Apt-RPC, (E) reflectance spectra of Apt-RPC upon adding different concentrations of RBD solutions, (F) CIE plot of Apt-RPC towards 1000 ng of RBD solution (inset: the corresponding digital photograph).

$$\lambda_{max} = 1.63D\left(n_{eff}^2 - \sin^2\theta\right)^{\frac{1}{2}}$$

$$n_{eff}^2 = fn_p^2 + (1-f)n_{air}^2$$

where, n_{eff} is the effective refractive index of the material, D is diameter of microsphere, f is the volume fraction, n_{air} and n_p are refractive indices of air and RPC, respectively. According to the modified Bragg's law, λ_{max} is a function of microsphere diameter and effective refractive index of the PCs.[45] The UV-vis reflectance spectra of RPC and Apt-RPC are shown in Fig. 4D. The observed red-shift in the PBG position from 449 to 489 nm indicates the functionalization of the aptamer in RPC. The experiments were carried out in PBS buffer, and the reflectance spectrum of RPC in PBS (pH 7.4) was recorded to evaluate its interference in our studies, revealing a PBG shift to 475 nm, which is relatively lower than the spectral shift observed for Apt-RPC. This spectral shift observed in the RPC in PBS buffer was due to the swelling of the hydrogel shell.

Furthermore, we investigated the stimuli-responsive characteristics of Apt-RPC in relation to the receptor-binding

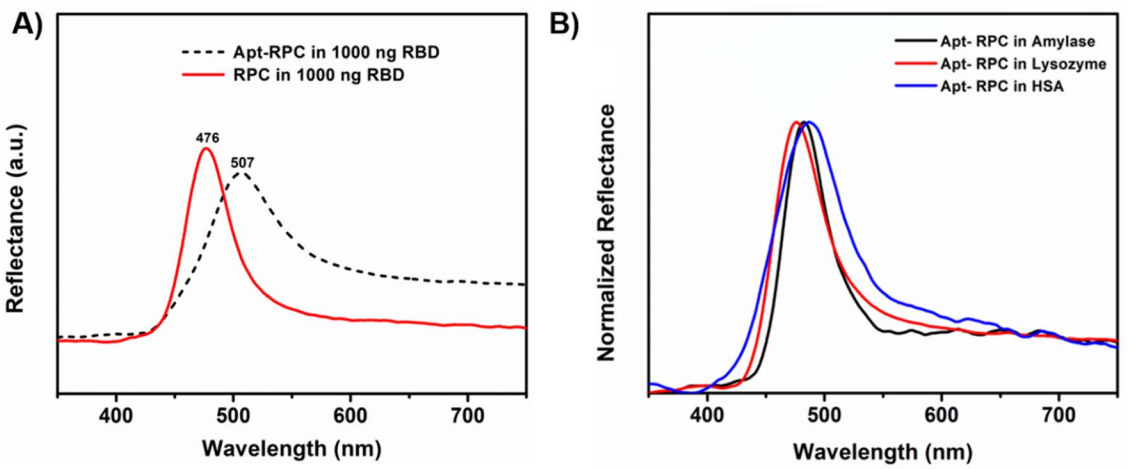

Fig. 5 (A) Reflectance spectra showing the response of Apt-RPC and RPC to 1000 ng of RBD, and (B) reflectance spectra of Apt-RPC in response to interferences such as amylase, lysozyme, and HSA.

domain (RBD) of the SARS-CoV-2 spike protein. Before conducting the sensing experiments, the Apt-RPC was rinsed with PBS to eliminate any unreacted aptamers. Different concentrations of RBD solution were prepared using 10 mM PBS buffer (pH 7.4). Approximately 30 μL of RBD solution at concentrations of 100, 500, 1000, and 1500 ng was applied to Apt-RPC, and reflectance spectra were recorded after 10 min. The corresponding reflectance spectra shown in Fig. 4E indicate a concentration-dependent spectral shift in response to the RBD. The initial Bragg diffraction wavelength of the RPC at 449 nm was red-shifted to 496, 501, and 507 nm when the concentration of RBD increased to 100, 500, 1000, and 1500 ng, respectively, resulting in an apparent color shift from violet to green. The detection range of the aptasensor was estimated to be, 100–1000 ng and no spectral difference was observed after 1000 ng. Fig. 4F illustrates the CIE plot subsequent to the addition of 1000 ng of RBD in Apt-RPC along with the corresponding visual color shift shown in the inset of Fig. 4F.

The fabricated aptasensor exhibited a rapid response to RBD, and the structure of the Apt-RPC film remained stable in the presence of RBD solution. A control experiment was conducted using non-functionalized RPC to validate the role of the aptamer in RPC binding to RBD. Fig. 5A shows the reflectance spectra of the aptamer-functionalized RPC (Apt-RPC) and non-functionalized RPC in a 1000 ng solution of RBD. The reflection spectra exhibited distinct peaks, indicating the specific interaction between RBD and the aptamer, which resulted in a noticeable red-shift of Apt-RPC in the RBD solution. Based on the above experimental results, the red-shift in the PBG of the Apt-RPC towards the RBD of the SARS-CoV-2 S-protein resulted from a network of hydrogen bonds between T42, T43, and T43 of the aptamer with Thr500, Gln506, and Asn437 from the RBD. Additionally, the conformational changes of the aptamer upon binding with the RBD lead to swelling of the Apt-RPC, resulting in increased interparticle spacing within RPCs and a red-shift.[44]

To detect SARS-CoV-2, swabs were collected from the nasal mucus and saliva. Therefore, selectivity studies were performed using a few model proteins present in nasal mucus and saliva for the practical application of the Apt-RPC sensor. Fig. 5B shows the reflection spectra of HSA, lysozyme and amylase. The HSA, lysozyme, and amylase concentrations were comparable to the range of human physiological conditions (1 mg mL^{-1}). The PBG of Apt-RPC towards HSA at 480 nm, lysozyme at 478 nm, and amylase at 475 nm was observed in the reflection spectra. This indicates that only RBD can selectively bind to Apt-RPC and induce significant red-shift diffraction, indicating the selectivity of the sensor. The reflection spectra revealed that the PBG of the Apt-RPC for HSA at 480 nm, lysozyme at 478 nm, and amylase at 475 nm clearly demonstrate that only the RBD can selectively bind to Apt-RPC, resulting in a noticeable red-shift in diffraction, demonstrating the selectivity of the sensor.

Conclusions

In summary, we adopted a straightforward method for the synthesis and fabrication of PS@poly(HEMA–AA) core–shell microsphere-based stimuli-responsive photonic crystals as an aptasensor platform for the specific detection of the RBD of the SARS-CoV-2 S protein. The specific binding of RBD to the aptamer resulted in hydrogel swelling, accompanied by a rapid color change (1 min) and a corresponding shift in the PBG, which enabled the detection of the RBD of the SARS-CoV-2 S-protein. The CIE plot showed a rapid visual color shift from violet to green upon the addition of RBD of SARS-CoV-2-S-protein to the Apt-RPC aptasensor, with a detection range of, 100–1000 ng. Compared to other COVID-19 detection methods, the developed biosensor uses a simple and facile approach for the visual detection of SARS-CoV-2 S-protein. We demonstrate this method as a qualitative approach for pathogen detection through the integration of a polymer-based aptasensor. Furthermore, the ability to modulate the PBG across the visible spectrum enhances the potential applications of this stimuli-responsive photonic crystal-based aptasensor in future biosensing technologies.

Experimental section

Materials and reagents

Styrene, 2-hydroxyethyl methacrylate (HEMA), acrylic acid (AA), ethylene glycol dimethacrylate (EGDMA), potassium persulfate (KPS), human serum albumin, lysozyme, amylase, 1-ethyl-3-(3-dimethyl aminopropyl)carbodiimide (EDC), and *N*-hydroxysuccinimide (NHS) were purchased from Sigma-Aldrich. All reagents were of analytical grade and used as received, without further purification. Single-stranded-DNA aptamer for the selective binding of RBD of SARS-CoV-2 (5′-CAG CAC CGA CCT TGT GCT TTG GGA GTG CTG GTC CAA GGG CGT TAA TGG ACA-3′) was purchased from Integrated DNA Technologies (IDT, India). All experiments were performed using ultrapure water (18.2 MΩ cm, Merck) from a Milli-Q ultrafiltration system.

Synthesis of core–shell microspheres and fabrication of CPCs

Monodispersed core–shell (CS) microspheres of polystyrene@poly(hydroxyethyl methacrylate–acrylic acid) [PS@poly(HEMA–AA)] were synthesized *via* emulsifier-free emulsion polymerization. Briefly, 5.07 mmol of HEMA, 4.5 mmol of AA, 57.5 mmol of styrene, and 0.53 mmol of EGDMA, which acted as a cross-linker, were mixed with 100 mL deionized water, placed in a round-bottomed flask, and placed in an oil bath at 70 °C. After 30 min, 0.07 mmol of potassium persulfate (KPS) (initiator) was introduced into the reaction mixture. Polymerization was carried out under a N_2 gas atmosphere with gentle magnetic stirring at 75 °C for 10 h. The resultant colloidal suspension was purified *via* centrifugation at 10 000 rpm for 30 min, and the purified CS microspheres were used to fabricate CPCs using the vertical deposition approach on glass substrates. Prior to deposition, the glass substrates were cleaned with ethanol, followed by N_2 plasma treatment to generate hydrophilic surfaces.

Fabrication of aptasensor based on RPC (Apt-RPC)

The functionalization of the aptamer on RPC was carried out using EDC/NHS coupling chemistry. The carboxyl functional groups on the CS microspheres of RPC were activated with EDC/NHS using 1 mL of phosphate-buffered saline (PBS, pH 7.4) containing 0.5 mM EDC and 0.5 mM NHS for an hour at ambient temperature. To the activated RPC, 30 μL of 500 nM aptamer in 2 mM PBS buffer solution was added, incubated at room temperature for 30 min, and stored overnight at 4 °C. The synthesized Apt-RPC sensor was subsequently rinsed with PBS to remove unreacted aptamers and used for subsequent investigations. Various quantities of RBD solutions in 10 mM PBS (pH 7.4) were introduced into the Apt-RPC sensor, and the reflectance spectra were recorded.

Characterizations

The morphology and dimensions of the CS microspheres were analyzed using transmission electron microscopy (TEM; JEOL JEM F 200). The hydrodynamic diameter was obtained using dynamic light scattering (DLS, Zetasizer Nano ZS, Malvern Instruments). Chemical functionalization studies were conducted using an FT-IR spectrometer (PerkinElmer) and X-ray photoelectron spectroscopy (XPS, PHI 5000 Versa Probe II ULVAC-PHI Inc., USA). Scanning electron microscopy (SEM) was performed using a Zeiss EVO 18 SEM (Germany). The reflectance spectra of the CPCs were obtained using a modular fiber-optic spectrophotometer (Ocean Optics DH-2000-BAL). We adopted the CIE (International Commission on Illumination) color space chromaticity diagram to validate the visual colors of the CPCs.

Conflicts of interest

The authors declare no conflicts of interest.

Data availability

All data supporting this study are included in this article. Additional data are available from the corresponding author upon reasonable request.

Acknowledgements

The authors thank Mr Kiran Mohan and Mr Harish Raj V. for the TEM and SEM acquisitions, respectively. MMT, PRC, and LL thank CSIR-SRF, SERB-National Post-doctoral Fellowship, and DST-INSPIRE fellowship, respectively, for financial support. This work was supported by the Council of Scientific and Industrial Research (CSIR, India).

References

1 F. Wu, S. Zhao, B. Yu, Y. M. Chen, W. Wang, Z. G. Song, Y. Hu, Z. W. Tao, J. H. Tian, Y. Y. Pei, M. L. Yuan, Y. L. Zhang, F. H. Dai, Y. Liu, Q. M. Wang, J. J. Zheng, L. Xu, E. C. Holmes and Y. Z. Zhang, *Nature*, 2020, **579**, 265–269.

2 L. A. Jackson, E. J. Anderson, N. G. Rouphael, P. C. Roberts, M. Makhene, R. N. Coler, M. P. McCullough, J. D. Chappell, M. R. Denison, L. J. Stevens, A. J. Pruijssers, A. McDermott, B. Flach, N. A. Doria-Rose, K. S. Corbett, K. M. Morabito, S. O'Dell, S. D. Schmidt, P. A. Swanson, M. Padilla, J. R. Mascola, K. M. Neuzil, H. Bennett, W. Sun, E. Peters, M. Makowski, J. Albert, K. Cross, W. Buchanan, R. Pikaart-Tautges, J. E. Ledgerwood, B. S. Graham and J. H. Beigel, *N. Engl. J. Med.*, 2020, **383**, 1920–1931.

3 P. Zhou, X. L. Yang, X. G. Wang, B. Hu, L. Zhang, W. Zhang, H. R. Si, Y. Zhu, B. Li, C. L. Huang, H. D. Chen, J. Chen, Y. Luo, H. Guo, R. Di Jiang, M. Q. Liu, Y. Chen, X. R. Shen, X. Wang, X. S. Zheng, K. Zhao, Q. J. Chen, F. Deng, L. L. Liu, B. Yan, F. X. Zhan, Y. Y. Wang, G. F. Xiao and Z. L. Shi, *Nature*, 2020, **579**, 270–273.

4 G. Bonaccorsi, F. Pierri, M. Cinelli, F. Porcelli, A. Galeazzi, A. Flori, A. L. Schmidt, C. M. Valensise, A. Scala, W. Quattrociocchi and F. Pammolli, *Sustainability*, 2022, **14**, 9699.

5 E. C. Holmes, *Annu. Rev. Virol.*, 2024, **11**, 21–42.

6 S. Steiner, A. Kratzel, G. T. Barut, R. M. Lang, E. A. Moreira, L. Thomann, J. N. Kelly and V. Thiel, *Nat. Rev. Microbiol.*, 2024, **22**, 206–225.
7 U. Lele and S. Goswami, *Med. Res. Arch.*, 2024, **12**(2), DOI: 10.18103/MRA.V12I2.5039.
8 J. Y. Choi and D. M. Smith, *Yonsei Med. J.*, 2021, **62**, 961.
9 M. Alexandridi, J. Mazej, E. Palermo and J. Hiscott, *Cytokine Growth Factor Rev.*, 2022, **63**, 1–9.
10 K. Sun, J. N. Bhiman, S. Tempia, J. Kleynhans, V. S. Madzorera, Q. Mkhize, H. Kaldine, M. L. McMorrow, N. Wolter, J. Moyes, M. Carrim, N. A. Martinson, K. Kahn, L. Lebina, J. D. du Toit, T. Mkhencele, A. von Gottberg, C. Viboud, P. L. Moore, C. Cohen, A. Buys, M. Carrim, L. de Gouveia, M. du Plessis, J. du Toit, F. X. Gómez-Olivé, K. P. Kgasago, R. Kotane, M. L. McMorrow, T. Moloantoa, S. Tollman, A. von Gottberg, F. Wafawanaka and N. Wolter, *Nat. Med.*, 2024, **30**, 2805–2812.
11 R. Liu, L. He, Y. Hu, Z. Luo and J. Zhang, *Chem. Sci.*, 2020, **11**, 12157–12164.
12 M. L. Wong and J. F. Medrano, *Biotechniques*, 2005, **39**, 75–85.
13 Q. Lin, D. Wen, J. Wu, L. Liu, W. Wu, X. Fang and J. Kong, *Anal. Chem.*, 2020, **92**, 9454–9458.
14 J. Huang, J. Wen, M. Zhou, S. Ni, W. Le, G. Chen, L. Wei, Y. Zeng, D. Qi, M. Pan, J. Xu, Y. Wu, Z. Li, Y. Feng, Z. Zhao, Z. He, B. Li, S. Zhao, B. Zhang, P. Xue, S. He, K. Fang, Y. Zhao and K. Du, *Anal. Chem.*, 2021, **93**, 9174–9182.
15 Y. Huang, C. Yang, X. f. Xu, W. Xu and S. w. Liu, *Acta Pharmacol. Sin.*, 2020, **41**, 1141–1149.
16 R. Yan, Y. Zhang, Y. Li, L. Xia, Y. Guo and Q. Zhou, *Science*, 2020, **367**, 1444–1448.
17 P. Dhar, R. M. Samarasinghe and S. Shigdar, *Int. J. Mol. Sci.*, 2020, **21**, 2485.
18 B. Ju, Q. Zhang, J. Ge, R. Wang, J. Sun, X. Ge, J. Yu, S. Shan, B. Zhou, S. Song, X. Tang, J. Yu, J. Lan, J. Yuan, H. Wang, J. Zhao, S. Zhang, Y. Wang, X. Shi, L. Liu, J. Zhao, X. Wang, Z. Zhang and L. Zhang, *Nature*, 2020, **584**, 115–119.
19 G. Yang, Z. Li, I. Mohammed, L. Zhao, W. Wei, H. Xiao, W. Guo, Y. Zhao, F. Qu and Y. Huang, *Signal Transduction Targeted Ther.*, 2021, **6**, 1–4.
20 M. Sun, S. Liu, X. Wei, S. Wan, M. Huang, T. Song, Y. Lu, X. Weng, Z. Lin, H. Chen, Y. Song and C. Yang, *Angew. Chem., Int. Ed.*, 2021, **60**, 10266–10272.
21 L. Zhang, X. Fang, X. Liu, H. Ou, H. Zhang, J. Wang, Q. Li, H. Cheng, W. Zhang and Z. Luo, *Chem. Commun.*, 2020, **56**, 10235–10238.
22 Z. Wang, S. Liu, Z. Shi, D. Lu, Z. Li and Z. Zhu, *Talanta*, 2024, **277**, 126318.
23 L. Wei, D. Zhu, Q. Cheng, Z. Gao, H. Wang and J. Qiu, *Food Res. Int.*, 2024, **179**, 114005.
24 F. Li, J. Lu, J. Liu, C. Liang, M. Wang, L. Wang, D. Li, H. Yao, Q. Zhang, J. Wen, Z. K. Zhang, J. Li, Q. Lv, X. He, B. Guo, D. Guan, Y. Yu, L. Dang, X. Wu, Y. Li, G. Chen, F. Jiang, S. Sun, B. T. Zhang, A. Lu and G. Zhang, *Nat. Commun.*, 2017, **8**, 1–14.
25 Q. Liu, W. Zhang, S. Chen, Z. Zhuang, Y. Zhang, L. Jiang and J. S. Lin, *J. Biol. Eng.*, 2020, **14**, 1–13.
26 Z. Li, X. Zhou, J. Yang, B. Fu and Z. Zhang, *ACS Appl. Mater. Interfaces*, 2019, **11**, 21417–21423.
27 P. Shen, W. Li, Y. Liu, Z. Ding, Y. Deng, X. Zhu, Y. Jin, Y. Li, J. Li and T. Zheng, *Anal. Chem.*, 2017, **89**, 11862–11868.
28 G. Isapour and M. Lattuada, *Adv. Mater.*, 2018, **30**, 1707069.
29 Y. Fang, B. M. Phillips, K. Askar, B. Choi, P. Jiang and B. Jiang, *J. Mater. Chem. C*, 2013, **1**, 6031–6047.
30 M. Jia, L. Yu, X. Li, Y. Li, X. He, L. Chen and Y. Zhang, *Talanta*, 2023, **260**, 124638.
31 I. Kalsoom, K. Shehzadi, M. Irfan, L. Qiu, Y. Wang, Z. Xu and Z. Meng, *Biosens. Bioelectron.*, 2025, **273**, 117091.
32 C. Fenzl, T. Hirsch and O. S. Wolfbeis, *Angew. Chem., Int. Ed.*, 2014, **53**, 3318–3335.
33 N. Griffete, H. Frederich, A. Maître, S. Ravaine, M. M. Chehimi and C. Mangeney, *Langmuir*, 2012, **28**, 1005–1012.
34 M. M. Thomas, P. R. Chandran, V. V. Vipin, A. P. Mohamed, P. Kingshott and S. Pillai, *React. Funct. Polym.*, 2021, **158**, 104779.
35 G. Hwang, G. Bak, Y. Kim, S. H. Jung, H. Na and Y. J. Jung, *ACS Omega*, 2025, **10**, 36582–36591.
36 G. Feng, K. Li, G. Li, Z. Zhang, J. Xiang, T. Chen, F. Jiao and H. Zhao, *ACS Appl. Polym. Mater.*, 2025, **7**(7), 4270–4278.
37 B. F. Ye, Y. J. Zhao, Y. Cheng, T. T. Li, Z. Y. Xie, X. W. Zhao and Z. Z. Gu, *Nanoscale*, 2012, **4**, 5998–6003.
38 H. Xuan, J. Ren, Y. Zhu, B. Zhao and L. Ge, *RSC Adv.*, 2016, **6**, 36827–36833.
39 G. Murtaza, A. S. Rizvi, M. Xue, L. Qiu and Z. Meng, *Anal. Chem.*, 2023, **95**(2), 917–923.
40 P. A. Lovell and F. J. Schork, *Biomacromolecules*, 2020, **21**, 4396–4441.
41 W. Wang, Y. Zhou, L. Yang, X. Yang, Y. Yao, Y. Meng and B. Tang, *Adv. Funct. Mater.*, 2022, **32**(40), 2204744.
42 L. Hu, Y. Wan, Q. Zhang and M. J. Serpe, *Adv. Funct. Mater.*, 2020, **30**, 1903471.
43 X. Jia, T. Zhang, J. Wang, K. Wang, H. Tan, Y. Hu, L. Zhang and J. Zhu, *Langmuir*, 2018, **34**, 3987–3992.
44 Y. Song, J. Song, X. Wei, M. Huang, M. Sun, L. Zhu, B. Lin, H. Shen, Z. Zhu and C. Yang, *Anal. Chem.*, 2020, **92**, 9895–9900.
45 F. Wang, Z. Meng, F. Xue, M. Xue, W. Lu, W. Chen, Q. Wang and Y. Wang, *Trends Environ. Anal. Chem.*, 2014, **3–4**, 1–6.